Universal Design Principles for Cascade Heterojunction Solar Cells with High Fill Factors and Internal Quantum Efficiencies Approaching 100%

*Adam Barito, Matthew E. Sykes, Bingyuan Huang, David Bilby, Bradley Frieberg, Jinsang Kim, Peter F. Green, and Max Shtein**

Cascade heterojunction (CHJ) organic solar cells have recently emerged as an alternative to conventional bulk heterojunctions and series-connected tandems due to their significant promise for high internal quantum efficiency (IQE) and broad spectral coverage. However, CHJ devices thus far have also exhibited poor fill factor (FF), resulting in minimal enhancements (or even decreases) in power conversion efficiency (PCE) when compared with single heterojunction (SHJ) cells. In this study, the major variables controlling the CHJ maximum power point and FF are determined using a combinatorial approach. By matching the maximum power point voltage (V_{MPP}) of the constituent parallel-connected heterojunctions (subjunctions) and minimizing the injection barriers intrinsic to CHJs, high FF and PCE can be achieved. Optimized CHJ devices are demonstrated with >99% IQE in the interlayer and a 46% increase in PCE compared to a SHJ reference (4.1% versus 2.8%). Devices with a transparent exciton dissociation layer (EDL)/interlayer/acceptor structure are employed, such that each CHJ has absorption efficiency identical to its interlayer/acceptor SHJ counterpart. Using these results, a clear map of performance as a function of material parameters is developed, providing straightforward, universal design rules to guide future engineering of molecules and layer architectures for CHJ organic photovoltaic devices.

1. Introduction

Organic photovoltaics (OPVs) have attracted considerable scientific and technological attention for cost-effective solar energy harvesting with rapid energy payback.[1] However, when compared with their inorganic counterparts, OPVs still exhibit substantially lower short-circuit current densities (J_{sc}), owing largely to their limited coverage of the solar spectrum and non-radiative losses involving the diffusion and dissociation of strongly bound excitons during the photoconversion process. While the optical absorption length of typical organic materials used for active layers is ≈100 nm, the characteristic diffusion length (L_D) for photogenerated excitons is an order of magnitude lower (≈10 nm),[2] leading to an efficiency tradeoff with respect to layer thickness.[3]

Two major device architectures have been used to circumvent the absorption/diffusion tradeoff: bulk heterojunctions (BHJs)[4] and vertically stacked, series-connected tandem devices.[5,6] In BHJs, the active layers are intermixed to create a spatially distributed heterojunction. With careful morphological control, the size of any donor or acceptor domain within the bulk can be decreased to less than the active materials' L_D. Without the thickness limitation by L_D, the active layer thickness can be increased to improve absorption efficiency, although this can lead to an increase in non-geminate recombination.[7] Furthermore, control of the BHJ active layer morphology remains the primary challenge for both device optimization and materials design. In the case of series tandems, multiple subcells with complementary absorption peaks are used to achieve higher absorption efficiency across the visible spectrum. The latter approach is generalizable, as the subcells in principle can comprise either planar or bulk heterojunctions. However, because tandem devices are connected electrically in series, the resulting device performance is voltage-additive and current-limited by the lowest current of either subcell.[6]

A new approach to circumventing the absorption/diffusion tradeoff involves cascade heterojunction (CHJ) devices.[8–10] In CHJs, the highest occupied molecular orbital (HOMO) and lowest unoccupied molecular orbital (LUMO) levels of three or more active layers are progressively offset to create multiple energetically cascading heterojunctions within the device. In the simplest case, a planar CHJ employs a three-layer architecture consisting of a donor/interlayer/acceptor stack: the interlayer

A. Barito, M. E. Sykes, B. Huang, D. Bilby, Prof. J. Kim, Prof. P. F. Green, Prof. M. Shtein
Materials Science and Engineering
University of Michigan
Ann Arbor, MI 48109, USA
E-mail: mshtein@umich.edu
B. Frieberg
Macromolecular Science and Engineering
University of Michigan
Ann Arbor, MI 48109, USA

DOI: 10.1002/aenm.201400216

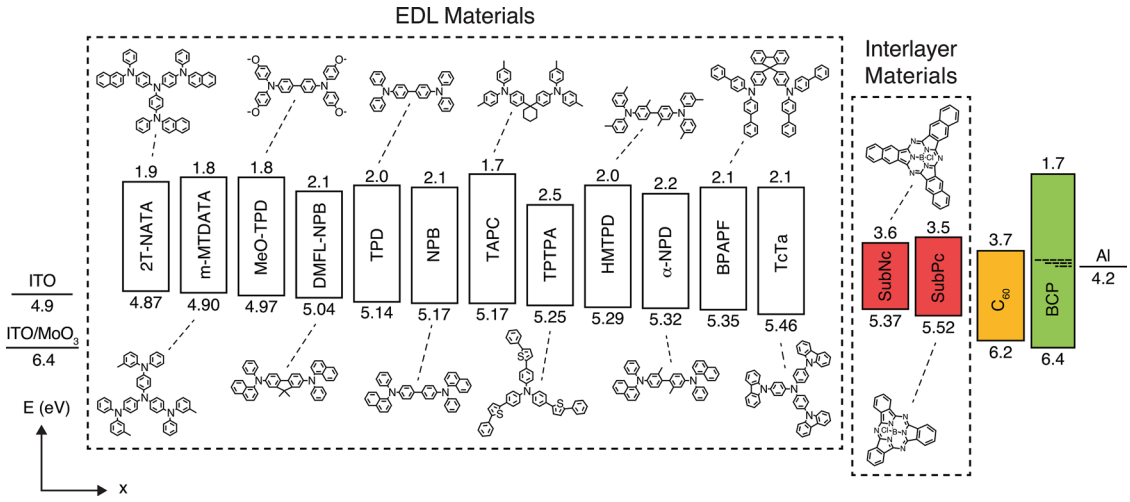

Figure 1. Schematic of energy levels and molecular structures for all materials used in this study. HOMO levels of EDL and interlayer materials were measured using cylic voltammetry and bandgap energies were estimated from the absorption onset. The HOMO level of C_{60} was taken from literature and it's bandgap energy was estimated from the absorption onset.[16] Energy levels for BCP and the electrodes were taken from literature.[14] The prospective EDL materials were chosen such that their HOMO levels ranged semicontinously from approximately 4.9 eV to 5.5 eV. The two interlayers were chosen based on their differences in V_{MPP} when in SHJ configurations with C_{60}.

is sandwiched between two heterojunctions, enabling exciton dissociation on both the donor and acceptor sides, thereby reducing the distance excitons must travel before dissociating. This reduced diffusion distance can substantially increase the internal quantum efficiency (IQE) of the interlayer, resulting in a higher external quantum efficiency (EQE) and overall device J_{sc}. Compared to BHJs, planar devices can offer nearly 100% charge collection efficiency, more straightforward optimization of optical absorption, and more refined control over individual layer morphologies.[11] Due to the nature of CHJ device design, it is also possible to broaden spectral coverage by using three (or more) active layers with absorption peaks in non-overlapping regions of the spectrum, providing an alternative or complementary approach to series tandem configurations. However, efficient charge collection in CHJs does not automatically lead to a good fill factor (FF).[9,10] Indeed, in a previous study we demonstrated a 66% increase in the IQE and EQE of boron subphthalocyanine chloride (SubPc) by introducing a large bandgap, transparent exciton dissociation layer (EDL) between SubPc and the anode in a planar single heterojunction (SHJ) SubPc/C_{60} device.[10] Although the J_{sc} improved significantly, the overall PCE exhibited only a minimal increase due to a concomitant decrease in FF, leaving open questions as to the fundamental limitations of the CHJ solar cell architecture.

Here, we perform an extensive, highly systematic study of the EDL/interlayer/acceptor system to probe the underlying mechanisms that cause low FFs in CHJ devices. We use 12 exciton dissociation layers, coupled with SubPc or boron subnaphthalocyanine chloride (SubNc) as interlayers and C_{60} as the acceptor **Figure 1**. By definition, the FF is a simple way of relating J_{sc} and V_{oc} to the maximum power point (MPP):

$$FF = \frac{V_{MPP} J_{MPP}}{V_{oc} J_{sc}} \quad (1)$$

where V_{MPP} and J_{MPP} are the voltage and current at the MPP, respectively. However, while FF can be a useful metric for describing device performance, it can be imprecise or misleading if both J_{sc} and V_{oc} vary between the devices under consideration. We instead focus on the MPP for comparisons between devices with the understanding that if V_{MPP} and J_{MPP} are maximized, then FF will also be maximized. For CHJs, we clearly show that the V_{MPP} is limited by two major factors, both of which can lead to the onset of s-kink behavior in the current–voltage (J–V) characteristics of the devices. First, we demonstrate that the two active heterojunctions (which we term "subjunctions") in the cascade operate electrically in parallel,[10] with the maximum V_{MPP} of the CHJ limited by the lowest V_{MPP} of the two subjunctions. Second, we show that the V_{MPP} of a CHJ is further limited by the energy offset between the HOMO levels (ΔE_{HOMO}) of the hole transporting donor layer and interlayer. As ΔE_{HOMO} increases, the voltage at the maximum power point (V_{MPP}) decreases, leading to a lower FF and PCE. We attribute this parasitic effect to the introduction of an energetic charge injection barrier, which results in a space charge buildup within the device and a corresponding decrease in the built-in field.[12,13] Impressively, for optimized devices we observe an increase in the peak IQE of the SubPc and SubNc layers from 38% and 66% to 84% and >99%, respectively, over reference single heterojunction (SHJ) devices with no EDL. Furthermore, by matching the V_{MPP} of each subjunction and choosing an EDL with $\Delta E_{HOMO} \leq 0.2$ eV, we minimize any losses in V_{MPP} (and FF) and demonstrate a 46% enhancement in PCE for a SubNc CHJ over its SHJ reference device.

2. Results and Discussion

2.1. Active Layer Energy Levels and Device Architectures

Twelve different triphenylamine derivatives were used in this study as EDLs, selected based on their high hole mobilities,

transparency in the visible spectrum, and HOMO levels varying from ≈4.9 eV to ≈5.5 eV. Figure 1 depicts a schematic energy level diagram and the molecular structure for all materials used.[14–16] In Figure S1 (Supporting Information), we show the absorption coefficients for each material, with only the interlayers and C_{60} acceptor having absorption peaks in the visible spectral region. The two interlayer materials were chosen primarily due to their different characteristic V_{MPP} when paired with C_{60} in a SHJ configuration. As demonstrated below, the EDL/interlayer V_{MPP} often limits the CHJ V_{MPP}, so choosing a reference SHJ with a lower V_{MPP} can help match the V_{MPP} between the EDL/interlayer and interlayer/C_{60} subjunctions.

MoO_3 was used as an anode buffer layer in all SHJ and CHJ devices employing SubPc as an active layer. While MoO_3 quenches excitons in SubPc and other common OPV materials,[10,17] its high work function is necessary for sustaining the ≈1.1 V open-circuit voltage of SubPc/C_{60} devices. Moreover, MoO_3 causes virtually no changes to the optical field profiles within the device, unlike other commonly used buffer layers such as poly(ethylenedioxythiophene):poly(styrenesulfonate).[18] Because MoO_3 is not required for the lower V_{oc} (≈0.8 V) of SubNc/C_{60} devices, it was not used in SubNc/C_{60} SHJ or EDL/SubNc/C_{60} CHJ devices. MoO_3 was used for all EDL/SubNc SHJ devices to ensure the built-in field did not limit their V_{oc}. As will be seen below, all trends in device performance were independent of the anode.

2.2. Electrical Operation of CHJ Devices

To understand CHJ device operation, we must consider photocurrent generation under short-circuit conditions (determined by EQE) as well as the V_{MPP} and FF limitations of the device under forward bias. Previously, we showed that during operation at zero applied bias (**Figure 2**c), both subjunctions in a CHJ device act as current sources operating electrically in parallel, with a barrier-free extraction of charge carriers upon exciton dissociation.[10] Since modeling of the EQE in CHJs was demonstrated previously, we leave the majority of its discussion to the Supporting Information, where we provide a more in-depth focus on the comparison between SHJ and CHJ devices.

By treating the subjunctions as acting electrically in parallel,[10] we can fully consider the *J–V* characteristics of CHJ devices under forward bias. In series-connected tandem structures, the J_{MPP} of the complete device will be limited by the lowest J_{MPP} of its two (or more) subcells.[6] Analogously,

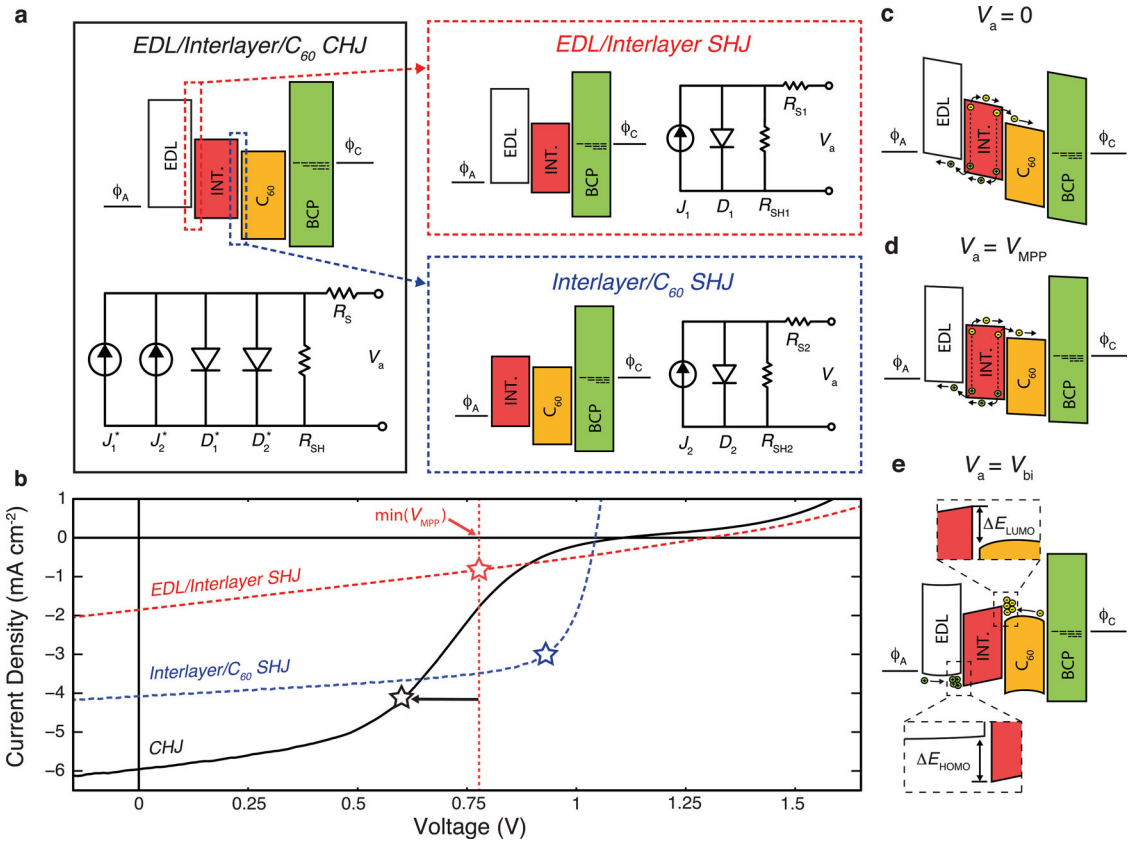

Figure 2. a) Schematic energy level and circuit diagrams for CHJ devices. The characteristic performance of each subjunction can be estimated by considering the *J–V* curves of corresponding SHJ devices. b) Characteristic experimental *J–V* curves of an EDL/interlayer SHJ, an interlayer/C_{60} SHJ, and an EDL/interlayer/C_{60} CHJ. The maximum power point for each device is marked by a star. From the two SHJs, it is clear the V_{MPP} of the EDL/interlayer will limit the maximum V_{MPP} of the CHJ device. Schematic band diagrams of c) exciton dissociation in a CHJ at short-circuit conditions ($V_a = 0$); d) exciton dissociation in a CHJ at V_{MPP}, where flat-band conditions have not been met; and e) field inversion at both subjunctions in a CHJ due to the introduced hole-injection barrier with energy ΔE_{HOMO}.

the V_{MPP} of a CHJ device will be limited by the lowest V_{MPP} of its constituent subjunctions. Due to CHJ device geometry, it is difficult to measure the V_{MPP} of each subjunction in situ. However, it is possible to estimate the V_{MPP} of each subjunction by measuring the J–V characteristics of each subjunction in separate SHJ configurations. These concepts are illustrated in Figure 2a, where equivalent circuit diagrams are provided for each SHJ device and the CHJ device comprised of the two corresponding subjunctions. Experimental J–V curves for an EDL/interlayer/acceptor (TAPC/SubPc/C_{60}) system are shown in Figure 2b. A star shape marks the maximum power point for each device. From this plot, we can see that the V_{MPP} of the EDL/interlayer subjunction will limit the V_{MPP} of the CHJ device. In all experimental results, as discussed further below, the V_{MPP} of the CHJ is less than or equal to the lowest V_{MPP} of the two operating subjunctions.

To minimize losses in CHJ devices, the V_{MPP} values of the subjunctions must be closely matched. Previous studies have shown that the most important factors in determining the V_{oc} of SHJ devices are the energy of the HOMO-LUMO gap (ΔE_{HL}) and the polaron pair binding energy (E_B) between the donor and acceptor layers. At best, V_{MPP} will be limited by the maximum V_{oc} of the SHJ, as determined by:

$$V_{oc,max} = \Delta E_{HL}/q - E_B \quad (2)$$

where q is the electron charge.[19] In **Figure 3**a, we plot V_{oc} versus ΔE_{HL} for all EDL/interlayer SHJ devices fabricated in this study. As expected, V_{oc} does increase with larger ΔE_{HL}, but E_B also appears to increase as ΔE_{HL} approaches the interlayer bandgap energy (i.e., $\Delta E_{HOMO} \approx 0$), especially in the case of the EDL/SubNc SHJ devices. This is consistent with experimental findings by Zhang et al.,[20] attributable to a linear dependence of the polaron pair separation distance (a_0) on ΔE_{HOMO}.[21] Figure 3b plots simulated V_{MPP} values versus E_B for a standard SubPc/C_{60} SHJ, with V_{MPP} values taken from photocurrent curves simulated using the Onsager-Braun model, as detailed in the Supporting Information.[22] Figure 3b shows that V_{MPP} scales linearly with E_B, with a 0.1 eV change in E_B causing a 45% drop in V_{MPP}. Thus we conclude that ΔE_{HL} and E_B (or a_0) are critical in matching the V_{MPP} of each subjunction in the CHJ.

2.3. Effect of ΔE_{HOMO} on CHJ V_{MPP}

As demonstrated in Figure 2b, the V_{MPP} of a CHJ can be lower than the V_{MPP} of either subjunction. To elucidate any other possible loss mechanisms, we investigated the effects of energy level alignment on CHJ V_{MPP}. It has been well established that injection barriers can lead to s-kink J–V behavior in OPVs, either due to non-ohmic contact at the electrode/donor interface[23] or injection bottlenecks between the p and i layers in p-i-n type OPV cells.[12,24] Because cascading energy levels are required for creating multiple heterojunctions, CHJs inherently contain more injection barriers than SHJs. In CHJs, injected holes and electrons could in principle recombine at either the EDL/interlayer heterojunction or the interlayer/acceptor heterojunction. In practice, however, asymmetric injection barriers and carrier mobilities will force recombination to occur at one of the subjunctions, which will in turn determine the overall diode behavior of the CHJ.[19,25] For devices in this study, and the majority of CHJs shown previously in literature, phthalocyanines have been used as the interlayer, resulting in a large mismatch between interlayer hole (μ_h) and electron (μ_e) mobilities. Because $\mu_h > \mu_e$ for most phthalocyanines, recombination of injected charges will preferentially occur at the interlayer/acceptor interface. Recombination at that interface is favored even more if the electron injection barrier from the acceptor into the interlayer (ΔE_{LUMO}) exceeds the hole injection barrier from the EDL into the interlayer (ΔE_{HOMO}), as is the case for devices in this study with $\Delta E_{HOMO} < 0.2$ eV (Figure 2e).

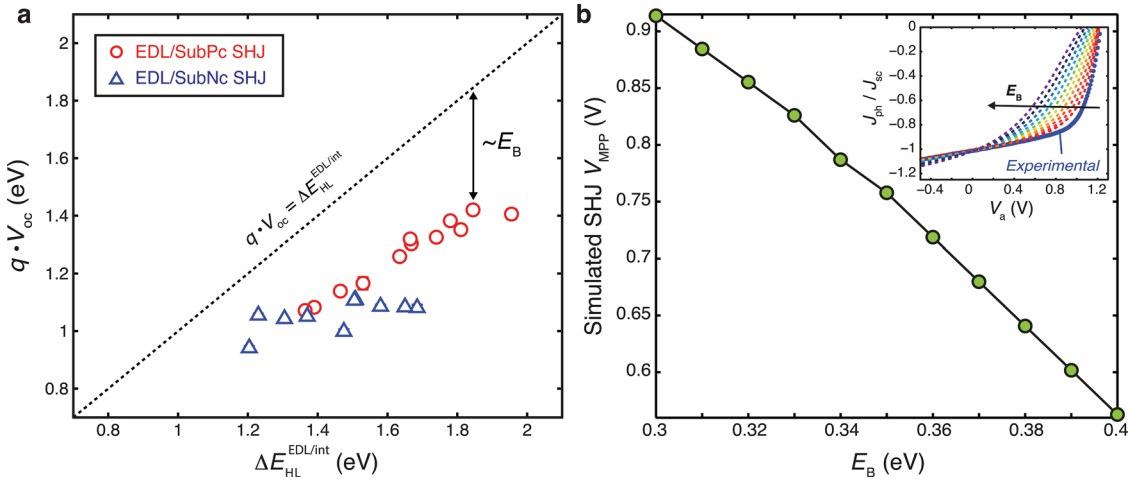

Figure 3. a) V_{oc} of every EDL/interlayer SHJ device in this study versus ΔE_{HL}. Error bars were calculated as one standard deviation of measurements from at least six devices, but are too small to show up in the plot. b) Simulated V_{MPP} for a SubPc/C_{60} SHJ as a function of polaron pair binding energy, E_B. Inset: Normalized calculated photocurrent curves vs. applied bias, for varying E_B. Simulated photocurrent and V_{MPP} values were calculated using an Onsager-Braun model, as detailed in the Supporting Information.

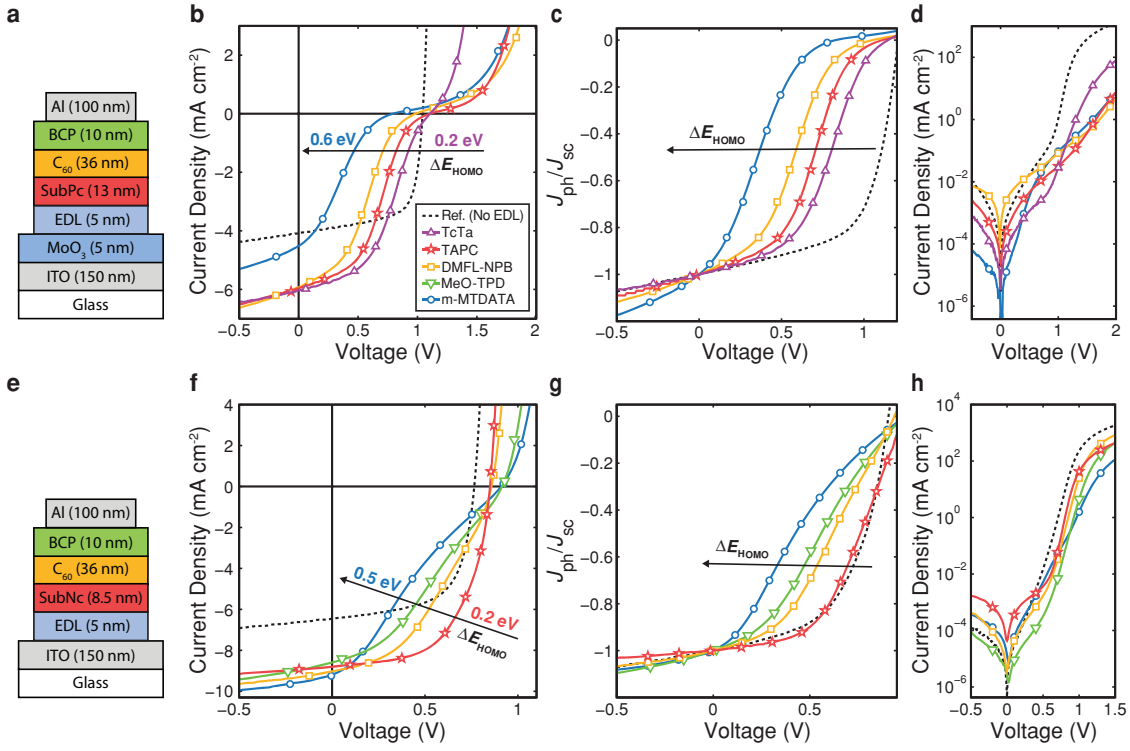

Figure 4. The effect of ΔE_{HOMO} on the *J–V* performance of CHJ devices. a–d) The device structures, *J–V*, normalized photocurrent, and dark current for devices using SubPc as the interlayer. The device structure for SubPc devices was (all thicknesses in nm) ITO/5 MoO_3/5 EDL/13 SubPc/36 C_{60}/10 BCP/100 Al. e–h) The same data for devices using SubNc as an interlayer. The SubNc device structure was ITO/5 EDL/8.5 SubNc/36 C_{60}/10 BCP/100 Al. Reference devices with no EDL are represented by dashed black lines.

If recombination occurs at the interlayer/acceptor interface, we must then consider the effect of the HOMO level offset, ΔE_{HOMO}, introduced by inserting the EDL layer. While this offset is necessary for enabling dissociation at the EDL/interlayer interface and creating a second heterojunction, it also introduces an additional hole injection barrier that can lead to a buildup of charge in the device and a subsequent decrease in the built-in field.[13] At zero bias (Figure 2c), Fermi level alignment in all layers provides band bending that is beneficial to dissociating excitons at each heterojunction; as such, the photocurrent contributions from each subjunction are perfectly additive. As V_a increases ($0 < V_a < V_{oc}$), exciton dissociation efficiency (η_{Diss}) decreases monotonically with the internal field until flat band conditions are reached. The maximum power point will occur at $V_a = V_{MPP}$, before flat band conditions (Figure 2d). Typically the field inside the active layers is assumed to be nearly constant below V_{oc}, although this is not necessarily the case in CHJs. Tress et al. employed a system using multiple hole transport layers and a transparent interlayer (called a donor layer in the study, as the only photocurrent-producing heterojunction was located at the interlayer/acceptor interface). Using a recursive transport model, ΔE_{HOMO} was shown to cause field inversion at the heterojunction (band bending in opposition to exciton dissociation), causing a sharp drop in η_{Diss}, shutting off photocurrent production before V_{oc} and causing s-kink behavior in the *J–V* curve (Figure 2e). However, in that study, both the HTL and "donor" layers were transparent, meaning that all photocurrent generation came from absorption in the acceptor (C_{60}) layer. In this study, we employ CHJ devices with photocurrent generation occurring at both subjunctions, but expect a similar behavior to occur. To verify, we now experimentally determine the dependence of CHJ V_{MPP} on ΔE_{HOMO}.

In **Figure 4**, we show how ΔE_{HOMO} can affect *J–V* performance by varying the material used for the 5 nm transparent EDL. Figure 4a–d and Figure 4e–h show *J–V* curves for CHJ devices using SubPc and SubNc as the interlayer, respectively. The black dashed line in each plot represents the reference interlayer/C_{60} SHJ device without an EDL. The onset of s-kink behavior is most apparent in Figure 4c and Figure 4g, where we normalize the photocurrent for each device to its own J_{sc}. This provides a useful metric for the shape of the device curve regardless of the J_{sc}, and more clearly illustrates that the onset of s-kink behavior in the device is due to field inversion (and resultant shutting down of photocurrent production) at $V_a < V_{oc}$. Furthermore, in comparing the *J–V* curves of the devices under no illumination, we note that the dark current at V_{oc} is 10–100× lower in the CHJs than in the SHJ reference device without an EDL. Lower dark currents at biases close to V_{oc} indicate a decrease in recombination of injected charges at the dominant heterojunction, providing further evidence for a buildup of holes at the EDL/interlayer interface. If injected holes are unable to reach the interlayer/C_{60} interface, they cannot recombine with injected electrons and contribute to dark current.

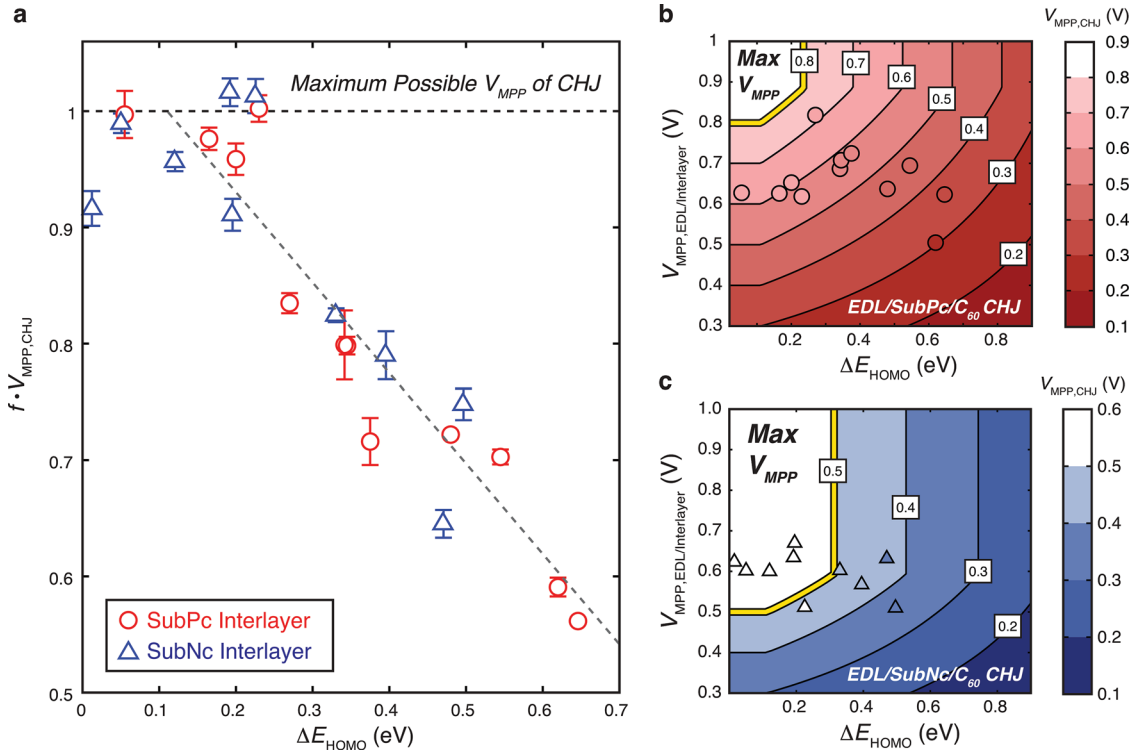

Figure 5. a) A plot of each CHJ V_{MPP} normalized by the minimum V_{MPP} of its constituent subjunctions versus ΔE_{HOMO} (as defined in (3)). The dashed horizontal line = 1 represents the maximum possible V_{MPP} of the CHJ based on each subcell. Beyond $\Delta E_{HOMO} \approx 0.2$ eV, the CHJ V_{MPP} is further lowered due to a decrease in V_{bi} (and therefore photocurrent) under forward bias. Error bars represent standard deviations calculated from six or more devices. b,c) Contour plots of simulated V_{MPP} for CHJ devices with SubPc and SubNc interlayers, respectively. CHJ V_{MPP} is determined by the minimum V_{MPP} of either subjunction and further decreased by ΔE_{HOMO}, dictated by the linear fit in (a), as given in (6). Experimental data points (circles and triangles) for CHJ devices are plotted and colored corresponding to their experimentally determined V_{MPP}.

2.4. Dependence of CHJ V_{MPP} on ΔE_{HOMO} and V_{MPP} of Subjunctions

To summarize the combined contributions of field inversion and voltage-limited operation, we measured the *J*–*V* performance of all EDL/interlayer and interlayer/C_{60} SHJ devices, extracting the V_{MPP} for each (performance parameters for all devices can be found in Table S2,S3, Supporting Information). **Figure 5**a plots the normalized V_{MPP} of each CHJ versus $\Delta E_{HOMO,}$ with the normalization factor f defined as:

$$f = \frac{1}{\min(V_{MPP}^{EDL/int}, V_{MPP}^{int/C60})} \quad (3)$$

where f is the inverse of the minimum V_{MPP} of either subjunction operating in the CHJ. Remarkably, the data collapse onto a universal trend, indicating that for $\Delta E_{HOMO} < 0.2$ eV, the CHJ is primarily limited by the lowest subjunction V_{MPP} and operates purely as a set of parallel diodes. However, for $\Delta E_{HOMO} > 0.2$ eV, the hole injection barrier becomes significant enough to shut down photocurrent production before V_{oc}, decreasing V_{MPP} below that of either subjunction. This 0.2 eV threshold is consistent with what has been shown in bilayer organic light-emitting diodes, where efficient hole injection into the electron transport layer occurs only when ΔE_{HOMO} is less than 0.1–0.3 eV.[26] Thus, Figure 5a encompasses the critical parameters that will determine the MPP (and thus PCE) of a CHJ device. From the plot, we conclude that for a high efficiency CHJ, the V_{MPP} of each subjunction must be closely matched and ΔE_{HOMO} between the EDL and interlayer should be kept below 0.2 eV.

We note that the HOMO levels of the EDL and interlayer materials were obtained via cyclic voltammetry on individual materials (detailed in the Experimental Section). Within the devices, however, the HOMO levels and offset energies could conceivably vary due to band bending or intermixing at the active layer interfaces. Therefore, as with the estimation of each subjunction's V_{MPP} from the V_{MPP} of its SHJ counterpart, the measured energy levels provide an approximate value that can be used for predicting CHJ device performance. It is likely that the variations in energy levels and V_{MPP} of each subjunction within the CHJs account for some of the data spread seen in Figure 5a.

2.5. Best Device Performance

In **Figure 6**, we show the device results for the best CHJs created from the combinatorial study using either a SubPc (solid red lines) or SubNc (solid blue lines) interlayer. Both data sets are compared to the reference interlayer/C_{60} SHJ devices, which are plotted with dashed lines. We note that these results

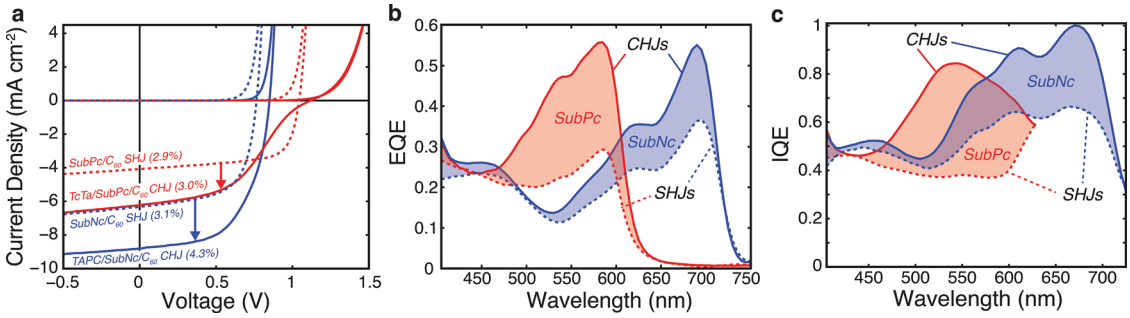

Figure 6. a) *J–V* curves, b) EQE, and c) IQE of optimized CHJ devices and the corresponding reference SHJ devices with no EDL. Results are shown for cascades with both SubPc and SubNc interlayers. IQE is defined as the experimental EQE divided by the modeled active layer absorption. The increase in J_{sc} in both CHJs can be explained by a substantial increase in the IQE and EQE of the interlayers. In the SubNc interlayer, the peak IQE is >99%. The more pronounced s-kink behavior in the SubPc CHJ is due to the limiting V_{MPP} of the TcTa/SubPc subjunction.

are consistent with those reported for SubPc/C_{60} and SubNc/C_{60} devices using other HTL materials.[27,28] Figure 6a shows that the J_{sc} for both CHJs is significantly higher than the J_{sc} of the respective reference devices due to the large increase in EQE (Figure 6b) and IQE (Figure 6c) of the interlayers. Here, we have defined the IQE as:

$$\mathrm{IQE}(\lambda) = \frac{\mathrm{EQE}(\lambda)}{\eta_{\mathrm{Abs}}(\lambda)} \tag{4}$$

where EQE(λ) is the experimentally determined external quantum efficiency of the device and $\eta_{\mathrm{Abs}}(\lambda)$ is the absorption of only the active layers at wavelength λ, as determined by optical modeling (fittings by the optical model are shown in Figure S2, Supporting Information). Impressively, the IQE of the SubNc interlayer within the cascade approaches 100% (>90% from 650–700 nm, with a peak value of >99%), meaning that nearly all photogenerated excitons in the SubNc are converted to electrical current. Furthermore, the V_{MPP} of the SubNc CHJ is insensitive to the insertion of a 5 nm TAPC EDL between the ITO anode and the SubNc layer, while the SubPc CHJ sees a large drop in V_{MPP}, consistent with a prior result.[9] Consequently, the FF of the SubNc/C_{60} SHJ (62%) is largely maintained in the TAPC/SubNc/C_{60} CHJ (58%), whereas the FF of the TcTa/SubPc/C_{60} CHJ (44%) decreases significantly compared to the SubPc/C_{60} SHJ (67%). This makes empirical sense, considering the V_{MPP} of each SubPc subjunction (0.63 ± 0.01 V for the TcTa/SubPc SHJ and 0.89 ± 0.01 V for the SubPc/C_{60} SHJ), with the TcTa/SubPc subjuncton limiting the overall V_{MPP} of the CHJ to 0.63 ± 0.01 V. On the other hand, the V_{MPP} of each SubNc subjunction is closely matched (0.63 ± 0.01 V for the TAPC/SubNc SHJ and 0.59 ± 0.01 V for the SubNc/C_{60} SHJ), leading to a CHJ V_{MPP} = 0.60 ± 0.01 V.

2.6. V_{oc} Limitations in CHJ Devices

Recently, Cnops et al. suggested that the V_{oc} of CHJs should be limited by the energy levels of the outermost active layers.[29] This limitation on the V_{oc} would occur due to the additional losses in energy as the free charges are extracted from the device. In **Figure 7**, we plot the V_{oc} of each CHJ versus $\Delta E_{HL}^{EDL/C60}$ (the difference in energy between the HOMO level of the EDL and the LUMO level of the C_{60} layer), and indeed we see that the V_{oc} can be limited for a small enough $\Delta E_{HL}^{EDL/C60}$. In the CHJ devices with a SubPc interlayer, we observe a crossover point at $\Delta E_{HL}^{EDL/C60} \approx 1.45$ eV ($\Delta E_{HOMO} \approx 0.35$ eV), above which the V_{oc} remains relatively constant, and below which the V_{oc} decreases monotonically with decreasing $\Delta E_{HL}^{EDL/C60}$. A similar transition is inferred at ≈1.18 eV ($\Delta E_{HOMO} \approx 0.48$ eV) for devices with a SubNc interlayer, however the limited data below this value makes it more approximate. Critically, any limitations in V_{oc} only occur for very small $\Delta E_{HL}^{EDL/C60}$ values. Conversely, for larger $\Delta E_{HL}^{EDL/C60}$ (smaller ΔE_{HOMO}) values, the CHJ devices actually exhibit an increase in V_{oc} compared to the reference interlayer/C_{60} SHJ, which we attribute to a decrease in dark current (Figure 4d,h). The black dotted line in Figure 7 represents:

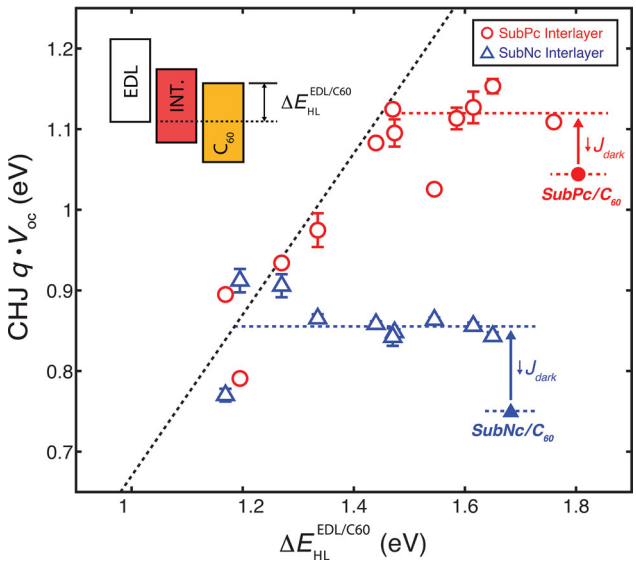

Figure 7. A plot of qV_{oc} for each CHJ device versus $\Delta E_{HL}^{EDL/C60}$ (the difference in energy between the HOMO and LUMO levels of the EDL and C_{60} layers, respectively). The V_{oc} of the CHJ devices increases initially upon insertion of an EDL due to a decrease in the dark current. As $\Delta E_{HL}^{EDL/C60}$ decreases, the V_{oc} of the CHJs remains relatively constant until it becomes limited by $\Delta E_{HL}^{EDL/C60} - E_B$. The diagonal black dotted line represents $\Delta E_{HL}^{EDL/C60} - 0.3$ eV, indicating a binding energy of 0.3 eV (consistent with the fitted E_B in the Supporting Information).

$$qV_{oc} = \Delta E_{HL}^{EDL/C60} - 0.3\text{eV} \quad (5)$$

indicating that the maximum possible V_{oc} of the CHJs is limited by $\Delta E_{HL}^{EDL/C60}$ and an effective binding energy of ≈0.3 eV, consistent with our calculated E_B of the SubPc/C_{60} and SubNc/C_{60} heterojunctions (Supporting Information). Since a majority of photocurrent in the CHJ is generated at the interlayer/C_{60} interface,[10] it is not surprising that the effective E_B of the CHJ is close to that of the interlayer/C_{60} subjunction.

As demonstrated by the EDL/SubNc/C_{60} devices, CHJs with interlayer/acceptor subjunctions exhibiting high recombination losses can employ donor layers with a larger ΔE_{HOMO} before V_{oc} begins to drop. However, as we have already established that ΔE_{HOMO} should be kept to less than 0.2 eV to minimize charge injection barriers in the devices, properly designed CHJs will not be voltage-limited. Instead, CHJ operation can substantially reduce recombination losses and bring the V_{oc} closer to the theoretical maximum.

2.7. Design Rules for CHJ Devices

The results presented in this study can guide future CHJ device design, principally dictating that ΔE_{HOMO} be less than 0.2 eV and the polaron pair binding energy be minimized for the EDL/interlayer interface. It is also possible now to screen materials systems for their utility in CHJ configurations. In Figure 5b,c, we extrapolate the relationship shown in Figure 5a to provide contour plots for predicting the V_{MPP} of an EDL/SubPc/C_{60} CHJ (Figure 5b) and an EDL/SubNc/C_{60} CHJ (Figure 5c) as a function of EDL/interlayer V_{MPP} and ΔE_{HOMO}. A linear fit of the universal trend in Figure 5a produces a general equation:

$$fV_{MPP,CHJ} = -(0.78eV^{-1})(\Delta E_{HOMO}) + 1.08 \quad (6)$$

with the caveat that the cascade V_{MPP} will not exceed the V_{MPP} of either subjunction. We note that (6) implies no dependence of V_{MPP} on other material properties such as charge mobility. In the Supporting Information, we consider such charge mobility effects and in fact show a strong correlation between HOMO level and hole mobility. However, we see no apparent dependence of CHJ V_{MPP} on EDL layer thicknesses, and thus conclude that any effects due to mobility are negligible or secondary to the injection barrier introduced by ΔE_{HOMO}. As an aside, the apparent relationship between HOMO level and hole mobility for these materials warrants further investigation, as it could provide further insight into previous studies with similar systems where changes in device performance were attributed primarily to variations in the hole mobility of the HTL.[27,30]

Finally, from comparing the two contour plots (Figure 5b,c), we can see that a much lower EDL/interlayer V_{MPP} is required to achieve maximum V_{MPP} in the SubNc CHJ as compared to the SubPc CHJ. In many cases, the simplest route to a high-performance CHJ device may be choosing a base device system with higher J_{sc} and lower V_{oc} or V_{MPP}. By "trading" J_{sc} for V_{MPP}, the PCE of the reference SHJ device can remain high, while lowering the required V_{MPP} of the introduced subjunction in the CHJ.

3. Conclusions

We have shown that CHJ architectures are viable options for high-efficiency planar OPVs, primarily due to their nearly 100% IQE within the interlayer. To ensure high fill factor, the V_{MPP} of each subjunction must be matched and the HOMO level offset between the EDL and interlayer should be <0.2 eV. Using these proposed design rules, we demonstrated a 46% increase in the power conversion efficiency of a SubNc/C_{60} planar device by introducing a transparent EDL between SubNc and the ITO anode (from 2.8% ± 0.2% to 4.1% ± 0.2%). By introducing the 5 nm layer of TAPC, the IQE of the SubNc layer increased from 66% to >99% at its peak, while the high fill factor of the SubNc/C_60 SHJ was largely maintained.

While the PCE was significantly enhanced in properly designed CHJs, J_{sc} could be improved further through increased active layer absorption. Because the presence of two heterojunctions relaxes the tradeoff between absorption and exciton diffusion, the interlayer thickness can be increased to maximize absorption. Some materials are more suitable for this than others; Verreet et al. recently showed that replacing C_{60} with hexachlorinated boron subphthalocyanine chloride allowed the SubNc layer thickness to increase upwards of 20 nm.[28] Furthermore, by using a smaller bandgap material in place of the transparent EDL to increase spectral coverage, device J_{sc} should increase without any additional drop in V_{oc}, V_{MPP}, or FF. Because the CHJ devices have such high IQE, they are also ideal candidates for use as sub-cells in series-connected tandems, potentially allowing for high efficiency OPVs comprising six or more active layers with complementary absorption peaks.

4. Experimental Section

Energy Levels: HOMO levels for all interlayer and EDL materials were measured via cyclic voltammetry. Each material was dropcast from chloroform onto a 3 mm diameter glassy carbon working electrode. Using 0.1 M tetrabutylammonium hexafluorophosphate in acetonitrile as an electrolyte, samples were scanned at a rate of 0.1 V s^{-1} relative to an $Ag/AgNO_3$ reference electrode with a Pt wire counter electrode. Scans were normalized to the onset of oxidation of ferrocene, taken as –4.8 eV. The bandgap was estimated from the onset of absorption, and the LUMO level was calculated by adding the bandgap to the HOMO level.

Device Fabrication: Devices were deposited on commercially available ITO (Delta Technologies, 150 nm thick, R_s < 15 Ω/□). Substrates were cleaned via heated (40 °C) sonication in detergent, water, acetone, trichloroethylene, and isopropanol, followed by boiling in isopropanol and 10 minutes of ultraviolet/ozone treatment to remove carbon residues and increase the anode work function. Device layers were deposited via vacuum thermal evaporation (VTE) using an Ångstrom AMOD deposition chamber. Fabrication and *J–V* testing was performed in a glovebox filled with an inert nitrogen environment (<1 ppm O_2 and H_2O). To minimize degradation in atmosphere during testing, devices were simultaneously deposited on three substrates, so that one of each could be used for testing *J–V*, EQE, and absorption. Only samples for EQE and absorption measurements were exposed to atmosphere. For EQE and *J–V* testing, aluminum island electrodes were deposited through a shadow mask with a diameter of 1 mm. All device areas were measured using a Carl Zeiss Scope A.1 optical microscope and included explicitly in calculating J_{sc}, EQE, IQE, and PCE. All organic materials were purchased from Luminescence Technology Corp. and deposited with no further purification. SubPc, SubNc, BCP, and all EDL materials (>99%) and C_{60} (>99.5%) were sublimed grade. MoO_3 (>99.99%) was purchased from Sigma Aldrich and Al (99.9%) was purchased from Alfa Aesar.

Device Characterization: Device *J–V* curves were recorded using an HP 4156B precision semiconductor parameter analyzer. The cells were illuminated with a Newport solar simulator (model# 91191–1000) calibrated to AM1.5 (100 mW cm^{-2}) using an NREL Si reference cell (Model PVM233 KG5). EQE was measured by directing a collimated beam of optically chopped light (185 Hz) from a halogen lamp coupled to a Newport 1/8m monochromator (5 nm FWHM) incident on the sample. The photocurrent was measured using a Stanford Research Systems SR530 lock-in amplifier and compared to the output from a calibrated Si photodiode. The spectrum of the solar simulator was measured with an Ocean Optics USB2000 spectrometer and convoluted with the experimental EQE to determine the spectral mismatch factor for each device with respect to the AM1.5G spectrum.[31] All mismatch factors were determined to be 1 ± 0.05. Absorption in the completed devices was measured in reflection mode using a Perkin Elmer Lambda 750 UV/Vis/NIR spectrometer at an incidence angle of 7.5°. The absorption spectrum for each device was then compared to a transfer matrix optical model to confirm device layer thicknesses. IQE was calculated by dividing experimental EQE by modeled active layer absorption at each wavelength at normal incidence.

Optical Properties of Materials: The thicknesses and optical properties of all materials were measured using a variable angle spectroscopic ellipsometer (M-2000, J.A. Woollam Co.). Measurements were performed in both transmission mode and reflection mode at angles of 55°, 65°, and 75° for each of the materials on a glass substrate. The film thickness and surface roughness were first determined by fitting the acquired ellipsometric angles Δ and Ψ to a Cauchy model over the wavelength range in which the material is transparent. The refractive index values were then determined by fixing the film thickness as well as surface roughness and parameterizing the material as a B-Spline layer. The wavelength range was gradually increased, in increments of 0.1 eV, until it included the entire measured spectral range. The resultant values were then verified to be Kramers-Kronig (KK) consistent.

Mobility Measurements: For hole mobility measurements, samples were fabricated with the structure ITO/PEIE(10 nm)/EDL(800 nm)/Au (80 nm). PEIE (0.4 wt% in methoxyethanol) was spin-coated at 5000 rpm for 60 s and subsequently baked at 100 °C for 10 min prior to VTE deposition of the EDL at 1 Å s^{-1}. Circular gold contacts were deposited at 1 Å s^{-1} and defined by a shadow mask. Time-of-flight measurements were performed using a nitrogen laser (VSL337 from Newport) with a wavelength of $\lambda = 337.1$ nm, an intensity per pulse of ≈120 μJ, and a pulse duration less than 4 ns, for photogeneration of charge carriers in the films (illuminated through the ITO substrate). A Keithley 2400 SourceMeter was used to apply constant voltage over devices, with the ITO cathode under positive bias to prevent charge injection. The current transients were then amplified using a FEMTO DLPCA-200 low noise current amplifier and recorded with a Tektronix TDS3052C digital oscilloscope.

Supporting Information

Supporting Information is available from the Wiley Online Library or from the author.

Acknowledgements

This work was supported by the U.S. Department of Energy (DOE), Office of Basic Energy Sciences, as part of the Center for Solar and Thermal Energy Conversion, an Energy Frontier Research Center (Award No. DE-SC0000957). A.B. thanks the NSF for partial support of this work via the National Science Foundation Graduate Student Research Fellowship under Grant No. 1256260. This article was modified after online publication. Errors in the labels in figure 2 were corrected.

Received: February 5, 2014
Revised: March 24, 2014
Published online: May 3, 2014

[1] a) S. E. Gledhill, B. Scott, B. A. Gregg, *J. Mater. Res.* **2011**, *20*, 3167; b) S. B. Darling, F. You, *RSC Adv.* **2013**, *3*, 17633; c) C. J. Brabec, *Sol. Energy Mater. Sol. Cells* **2004**, *83*, 273.

[2] a) P. Peumans, A. Yakimov, S. R. Forrest, *J. Appl. Phys.* **2003**, *93*, 3693; b) W. Chen, M. P. Nikiforov, S. B. Darling, *Energy Environ. Sci.* **2012**, *5*, 8045.

[3] a) C. W. Tang, *Appl. Phys. Lett.* **1986**, *48*, 183; b) B. A. Gregg, *J. Phys. Chem. B* **2003**, *107*, 4688.

[4] a) G. Yu, J. Gao, J. C. Hummelen, F. Wudl, A. J. Heeger, *Science* **1995**, *270*, 1789; b) G. Chen, H. Sasabe, Z. Wang, X. F. Wang, Z. Hong, Y. Yang, J. Kido, *Adv. Mater.* **2012**, *24*, 2768; c) R. Pandey, Y. Zou, R. J. Holmes, *Appl. Phys. Lett.* **2012**, *101*, 033308; d) J. J. M. Halls, C. A. Walsh, N. C. Greenham, E. A. Marseglia, R. H. Friend, S. C. Moratti, A. B. Holmes, *Nature* **1995**, *376*, 498.

[5] A. Yakimov, S. R. Forrest, *Appl. Phys. Lett.* **2002**, *80*, 1667.

[6] B. E. Lassiter, C. Kyle Renshaw, S. R. Forrest, *J. Appl. Phys.* **2013**, *113*, 214505.

[7] R. Pandey, R. J. Holmes, *Appl. Phys. Lett.* **2012**, *100*, 083303.

[8] a) G. Zhang, W. Li, B. Chu, L. Chen, F. Yan, J. Zhu, Y. Chen, C. S. Lee, *Appl. Phys. Lett.* **2009**, *94*, 143302; b) M. Sim, J. S. Kim, C. Shim, K. Cho, *Chem. Phys. Lett.* **2013**, *557*, 88; c) T. D. Heidel, D. Hochbaum, J. M. Sussman, V. Singh, M. E. Bahlke, I. Hiromi, J. Lee, M. A. Baldo, *J. Appl. Phys.* **2011**, *109*, 104502; d) Z. R. Hong, R. Lessmann, B. Maennig, Q. Huang, K. Harada, M. Riede, K. Leo, *J. Appl. Phys.* **2009**, *106*, 064511.

[9] K. Cnops, B. P. Rand, D. Cheyns, P. Heremans, *Appl. Phys. Lett.* **2012**, *101*, 143301.

[10] A. Barito, M. E. Sykes, D. Bilby, J. Amonoo, Y. Jin, S. E. Morris, P. F. Green, J. Kim, M. Shtein, *J. Appl. Phys.* **2013**, *113*, 203110.

[11] A. Foertig, A. Wagenpfahl, T. Gerbich, D. Cheyns, V. Dyakonov, C. Deibel, *Adv. Energy Mater.* **2012**, *2*, 1483.

[12] W. Tress, K. Leo, M. Riede, *Adv. Funct. Mater.* **2011**, *21*, 2140.

[13] D. Cheyns, J. Poortmans, P. Heremans, C. Deibel, S. Verlaak, B. Rand, J. Genoe, *Phys. Rev. B* **2008**, *77*.

[14] a) A. Kahn, N. Koch, W. Gao, *J. Polym. Sci. Part B: Polym. Phys.* **2003**, *41*, 2529; b) M. T. Greiner, M. G. Helander, W. M. Tang, Z. B. Wang, J. Qiu, Z. H. Lu, *Nat. Mater.* **2012**, *11*, 76.

[15] Z.-L. Guan, J. B. Kim, H. Wang, C. Jaye, D. A. Fischer, Y.-L. Loo, A. Kahn, *Org. Electron.* **2010**, *11*, 1779.

[16] M. S. Dresselhaus, G. Dresselhaus, P. C. Eklund, *Science of Fullerenes and Carbon Nanotubes*, Academic, Waltham, MA **1996**.

[17] X. Xiao, J. D. Zimmerman, B. E. Lassiter, K. J. Bergemann, S. R. Forrest, *Appl. Phys. Lett.* **2013**, *102*, 073302.

[18] Y.-C. Tseng, A. U. Mane, J. W. Elam, S. B. Darling, *Sol. Energy Mater. Sol. Cells* **2012**, *99*, 235.

[19] B. Rand, D. Burk, S. Forrest, *Phys. Rev. B* **2007**, 75.

[20] M. Zhang, H. Wang, C. W. Tang, *Appl. Phys. Lett.* **2010**, *97*, 143503.

[21] P. Peumans, S. R. Forrest, *Chem. Phys. Lett.* **2004**, *398*, 27.

[22] a) L. Onsager, *Phys. Rev.* **1938**, *54*, 554; b) C. L. Braun, *J. Chem. Phys.* **1984**, *80*, 4157.

[23] a) A. Wagenpfahl, D. Rauh, M. Binder, C. Deibel, V. Dyakonov, *Phys. Rev. B* **2010**, 82; b) M. Glatthaar, M. Riede, N. Keegan, K. Sylvester-Hvid, B. Zimmermann, M. Niggemann, A. Hinsch, A. Gombert, *Sol. Energy Mater. Sol. Cells* **2007**, *91*, 390; c) M. R. Lilliedal, A. J. Medford, M. V. Madsen, K. Norrman, F. C. Krebs, *Sol. Energy Mater. Sol. Cells* **2010**, *94*, 2018.

[24] C. Uhrich, D. Wynands, S. Olthof, M. K. Riede, K. Leo, S. Sonntag, B. Maennig, M. Pfeiffer, *J. Appl. Phys.* **2008**, *104*, 043107.

[25] a) N. C. Giebink, B. E. Lassiter, G. P. Wiederrecht, M. R. Wasielewski, S. R. Forrest, *Phys. Rev. B* **2010**, 82; b) N. C. Giebink, G. P. Wiederrecht, M. R. Wasielewski, S. R. Forrest, *Phys. Rev. B*

2010, 82; c) C. W. Schlenker, M. E. Thompson, *Chem. Commun.* **2011**, *47*, 3702.
[26] a) J. Yang, J. Shen, *J. Phys. D* **2000**, *33*, 1768; b) N. Matsumoto, C. Adachi, *J. Phys. Chem. C* **2010**, *114*, 4652; c) F. Liu, P. Paul Ruden, I. H. Campbell, D. L. Smith, *Appl. Phys. Lett.* **2011**, *99*, 123301.
[27] C. Kulshreshtha, G. W. Kim, R. Lampande, D. H. Huh, M. Chae, J. H. Kwon, *J. Mater. Chem. A* **2013**, *1*, 4077.
[28] B. Verreet, K. Cnops, D. Cheyns, P. Heremans, A. Stesmans, G. Zango, C. G. Claessens, T. Torres, B. P. Rand, *Adv. Energy Mater.* **2014**, DOI: 10.1002/aenm.201301413.
[29] K. Cnops, B. P. Rand, D. Cheyns, B. Verreet, M. A. Empl, P. Heremans, *Nat. Commun.* **2014**, *5*, 3406.
[30] C. Kulshreshtha, J. W. Choi, J.-k. Kim, W. S. Jeon, M. C. Suh, Y. Park, J. H. Kwon, *Appl. Phys. Lett.* **2011**, *99*, 023308.
[31] C. H. Seaman, *Sol. Energy* **1982**, *29*, 291.